

Interstitial-Electrons Composed Multiple-Fold Fermions and Insights on Catalytic Nature in Nanoporous Electride C12A7 : e⁻

Weizhen Meng,^{†,‡} Xiaoming Zhang,^{*,†,‡} Ying Liu,^{†,‡} Xuefang Dai^{†,‡}, Zhiming Yu^{*,§} and Guodong Liu^{*,†,‡},

[†]School of Materials Science and Engineering, Hebei University of Technology, Tianjin 300130, China.

[‡]State Key Laboratory of Reliability and Intelligence of Electrical Equipment, Hebei University of Technology, Tianjin 300130, China

[§]Key Lab of Advanced Optoelectronic Quantum Architecture and Measurement (MOE), and School of Physics, Beijing Institute of Technology, Beijing 100811, China.

Email: zhangxiaoming87@hebut.edu.cn; zhiming_yu@bit.edu.cn; gdliu1978@126.com

Abstract

Nanoporous $12\text{CaO}\cdot7\text{Al}_2\text{O}_3$ (C12A7: e⁻), known as a famous electride and electron source material, was recently proposed to boost catalytic activity in C12A7: e⁻-based catalysts. However, the fundamental mechanism on such catalytic enhancement keeps in debate currently. Here, by means of symmetry analysis and first-principles calculations, we discover that this famous electride material, surprisingly, hosts interstitial-electrons composed multiple-fold fermions that helps to understand the catalytic nature of C12A7: e⁻-based catalysts. The multiple-fold fermions contain a sixfold- and a fourfold- degenerate point, locating at high symmetric points near the Fermi energy. Remarkably, comparing with traditional Weyl/Dirac fermions, the multiple-fold fermions are found to show extremely longer Fermi arcs on the C12A7: e⁻ (001) surface. As the result, this surface is highly active and carries a relatively low Gibbs free energy ($\Delta G_{\text{H}^*} = 0.24$ eV) during the catalytic process. This ΔG_{H^*} is also much lower than typical Weyl/Dirac catalysts proposed previously. This work offers a guiding principle for understanding catalytic nature of electrides and topological quantum catalysts as well.

Keywords: Electrides, Multiple-fold fermions, Long Fermi arcs, Topological quantum catalysts

Topological materials ¹⁻⁵, as novel types of quantum matter, have attracted considerable research interests currently. Topological materials were initially focused on topological insulators with the insulating bulk state and conducting surface (or edge) states ^{1,2}. Soon after, topological classification has been extended to semimetals (metals), known as topological semimetals (metals) ⁶. Weyl semimetals ⁷⁻⁹ and Dirac semimetals ¹⁰⁻¹³ are such examples, characterized by twofold degenerate Weyl points and fourfold degenerate Dirac points near the Fermi energy. The low-energy excitations of Weyl (Dirac) semimetals can well analogize the Weyl (Dirac) fermions in high-energy physics. Recently, several topological semimetals have been proposed to hold novel quasiparticle excitations even not allowed in high-energy theory, including the threefold, sixfold, and eightfold degenerate ones ¹⁴⁻²⁰. Such multiple-fold fermions were theoretically and experimentally studied in several materials ¹⁴⁻²⁶, accompanied by novel physical properties. One example is sixfold fermion discovered in AlPt ²², showing peculiarly long surface Fermi arcs extending through the entire Brillouin zone.

Electrides ^{27,28}, as a special category of ionic solids, have been hotly studied because of their unique electronic behavior and valence states; that is, excess electrons present as anions occupying the interstitial positions of lattice. The excess electrons can not only locate in zero-dimensional (0D), but also in one-dimensional (1D) and two-dimensional (2D) spaces of the lattice ²⁹⁻³³. Due to the loosely bounded nature of the excess electrons, electrides usually exhibit low work function and high carrier mobility, making them applicable in thermionic emitters, electrodes, and catalysts ³⁴⁻³⁹. Recently, electrides with nontrivial band topology, known as topological electrides ⁴⁰⁻⁴², have received peculiar attentions. Several families of topological electrides were proposed ⁴⁰⁻⁴⁸, where the nontrivial band topology produces different topological phases such as topological insulator, Weyl/Dirac nodes, nodal lines and multiple-fold fermions. Especially, some topological electrides were proposed to show floating surface bands ⁴², drastically different from traditional topological materials.

Nanoporous material $12\text{CaO}\cdot7\text{Al}_2\text{O}_3$ (known as $\text{C12A7:}\text{e}^-$), initially synthesized in 2003⁴⁹, has been one of the most famous electrides. Unlike former electrides, $\text{C12A7:}\text{e}^-$ shows excellent thermal stability at room and higher temperature and good chemical stability against air and moisture⁴⁹⁻⁵¹. $\text{C12A7:}\text{e}^-$ possesses many fantasizing properties such as small work function, high electron concentration, and superconductivity⁵²⁻⁵⁵. Recently, $\text{C12A7:}\text{e}^-$ -based catalysts attracted intensive investigations⁵⁶⁻⁶¹. For example, it is evidenced that Pt or Ru catalysts armed by $\text{C12A7:}\text{e}^-$ support show a boost of activity in ammonia synthesis^{57,58,61}. The mechanism for high catalytic activity in electride-based catalysts has been long believed to arise from the low work function associated with the interstitial electrons^{57,58, 62-65}. However, several experiments told different stories. A recent work⁶⁶ on electride Ca_2N found the activity enhancement can preserve even after the Ca_2N is completely transformed into the Ca_2NH hydride, where interstitial electrons of electride are annihilated. Another experimental work⁶⁶ on studying Ru/ $\text{C12A7:}\text{e}^-$ catalyst, indicates that the surface-adsorbed hydrogen, rather than the hydride captured in the cages of electride $\text{C12A7:}\text{e}^-$, is responsible for the high catalytic activity. However, to date the fundamental mechanism on the enhanced activity in $\text{C12A7:}\text{e}^-$ -based catalysts are still unclear.

Targeting on this puzzling aspect, in current work we investigate the fundamental electronic structure of electride $\text{C12A7:}\text{e}^-$. We surprisingly find this electride shows a nontrivial band topology, with coexisting of a sixfold- and a fourfold- degenerate point near the Fermi level. These multiple-fold fermions are mostly contributed by interstitial electrons confined inside the hollow cages. These symmetry-protected fermions characterize Fermi arc surface states. Remarkably, the Fermi arcs on the $\text{C12A7:}\text{e}^-$ (001) surface almost traverse the entire surface Brillouin zone, which are significantly longer than traditional Weyl/Dirac counterparts. Consequently, $\text{C12A7:}\text{e}^-$ harbors a highly active (001) surface. By simulating the hydrogen evolution reaction (HER) on the surface, $\text{C12A7:}\text{e}^-$ exhibits the Gibbs free energy ($\Delta\text{G}_{\text{H}^*}$) as low as 0.24 eV, which is favorable for high-activity catalyst. Our work suggests that:

during catalytic process in C12A7: e^- , although bulk cages themselves are not so active, their encaged interstitial electrons would contribute multiple-fold fermions, which activate the surface with high catalytic performance by producing giant surface Fermi arcs.

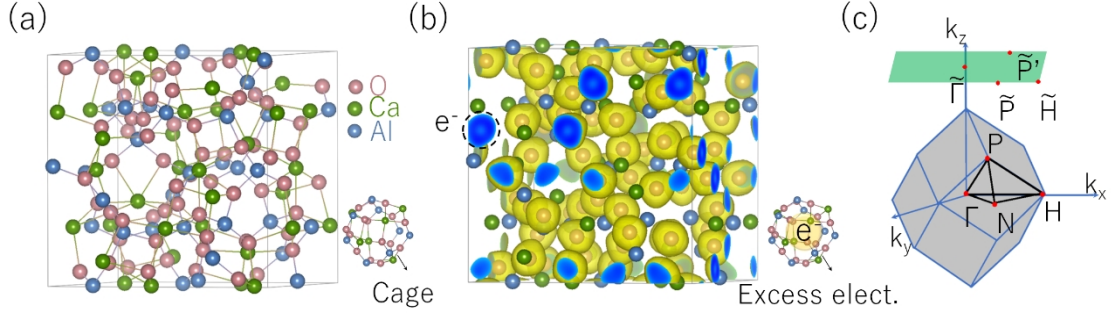


Fig. 1 (a) Crystal structure of electride C12A7: e^- . The cage in C12A7: e^- lattice is shown in the lower corner of the figure. (b) Electron localization function (ELF) of electride C12A7: e^- with the isosurface values set as 0.65. The lower corner of (b) shows the confined electrons inside the cage. (c) Bulk and the (001) surface Brillouin zone of electride C12A7: e^- with high symmetry points indicated.

We start by characterizing the crystal structure and the electride nature of C12A7: e^- . Figure 1(a) shows the unit cell of C12A7: e^- . It has a cubic structure and the space group belongs to $I\bar{4}3d$ (No. 220). C12A7: e^- is a nanoporous material, with one unit cell constructed by 12 cages with large lattice space (~ 0.4 nm in diameter for per cage). As depicted in the lower corner of Fig. 1(a), the cage is formed by the bonding among 6 Ca atoms, 7 Al atoms, and 16 O atoms. For the optimized crystal structure, the lattice constant yields to be $a = b = c = 10.48$ Å. The Ca atoms occupy the 24d Wyckoff sites; Al atoms occupy two Wyckoff sites including 12a and 16c; and O atoms occupy Wyckoff sites 16c and 48e, respectively. Specific Wyckoff coordinates are listed in Table SI in the [Supplementary Information](#). The optimized parameters well agree with the experiment values ⁴⁹. To capture the electride nature of C12A7: e^- , we show the electron localization function (ELF) in Fig. 1(b). One can observe that, a large region of electron is confined in the center of cages (the institute 12b Wyckoff

site), as shown by the circled region of Fig. 1(b). These results confirm C12A7: e^- is a typical 0D electride. In C12A7: e^- , the Ca, Al, and O atoms show +2, +3, and -2 valence states respectively. As the result, the material totally contains 4 excess electrons for a unit cell, and each cage shows the concentration fraction of 1/3 anionic electron. This scenario has been well identified by former experiments ⁴⁹.

We continue to investigate the electronic structure of C12A7: e^- based on density functional theory (DFT) ⁶⁷. More computational details can be found in the [Supplementary Information](#). Figure 2(a) shows the band structure and partial density of states (PDOSs) of C12A7: e^- . Considering that C12A7: e^- only contains light elements, the spin orbital coupling (SOC) is not included in the calculations. The impact of SOC on the band structure can be found in the [Supplementary Information](#). Figure 2(a) shows a metallic band structure of C12A7: e^- . Remarkably, we can observe band crossing points at the high symmetry points H and P near the Fermi level, as denoted by P_1 and P_2 , respectively. From the PDOSs shown in Fig. 2(a), we find the states near the Fermi level are mainly contributed by the interstitial electrons. This is also consistent with the orbital component analysis for bands near P_1 and P_2 [see the left panel of Fig. 2(b)]. In the right panel of Fig. 2(b), we show the partial electron density (PED) in the energy region of ± 0.02 eV around P_1 and P_2 . In these energy regions, we indeed observe large amounts of excess electrons locating inside the nanoporous cages.

Recently, an advanced work ⁶⁸ using topological quantum chemistry theory ⁶⁹ relates the topological aspects and electrides: the elementary band representations (BRs) can not only probe the nontrivial topology of electronic structures, but also identify the centers of electron density for specific bands (even for the floating bands from excess electrons). Based on this method, we perform the BRs analysis on the band crossings P_1 and P_2 . The results are shown in Table SI of the [Supplementary Information](#). The results show the bands for P_1 and P_2 are both formed by floating bands with BRs of A@12b, originating from the excess electrons inside the nanoporous cages (at the institute 12b Wyckoff sites). These outputs fully agree with

the results from DFT calculations in Fig. 2(b).

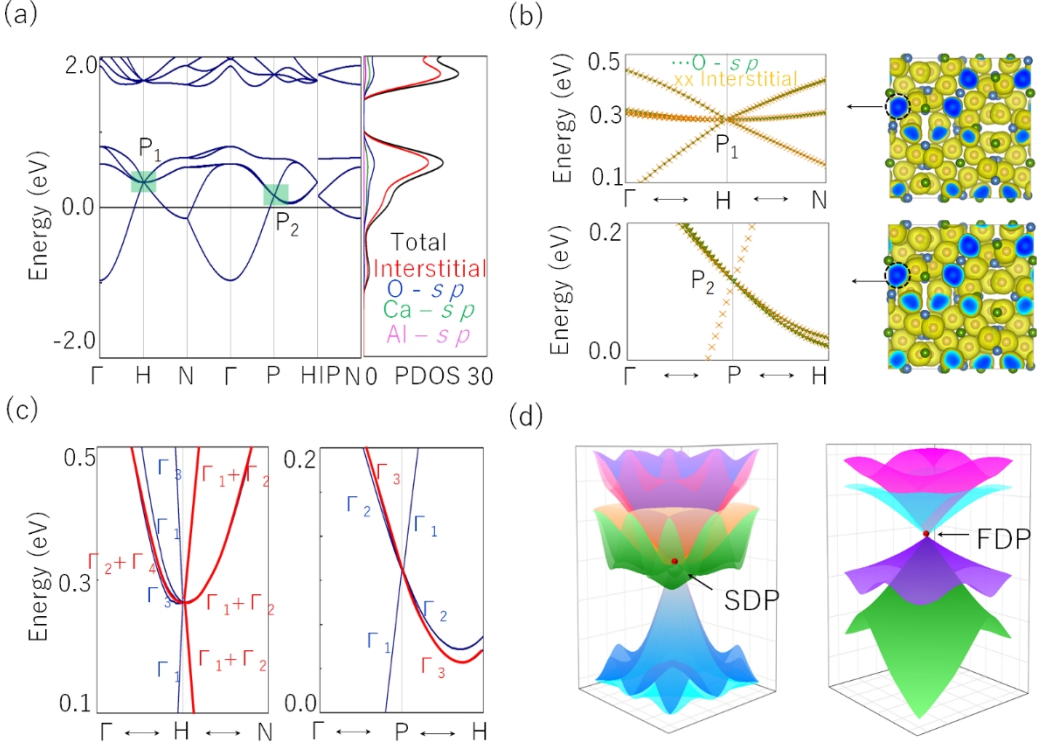


Fig. 2 (a) Band structure and partial density of states (PDOS) of electride C12A7: e^- . The Fermi level is set as zero energy. The band crossings at the H and P points are denoted as P_1 and P_2 . (b) The orbital-projected band structures near P_1 and P_2 are shown in the left panel. The right panel of (b) shows the partial electron density (PED) in the energy region of ± 0.02 eV around P_1 and P_2 . The isosurface value is chosen as 0.005 Bohr⁻³. (c) The enlarged band structures along with the irreducible representations near P_1 and P_2 . (d) The 3D plotting of band dispersions for the SDP and FDP.

To make further insights on P_1 and P_2 , we display the enlarged band structures along with the irreducible representations near P_1 and P_2 in Fig. 2(c). Detailed irreducible representations for other k -paths can be found in Table SII of the [Supplementary Information](#). Based on the symmetry analysis, we find P_1 at the H point is in fact a sixfold degenerate point (SDP), where the fatter bands are doubly degenerate while the thinner ones are singlets [see Fig. 2(c)]. Under similar analysis, the band crossing P_2 at the P point is a fourfold degenerate point (FDP). To be noted,

the FDP in C12A7: e^- is fundamentally different from traditional Dirac points, which will be discussed later. The 3D plotting of band dispersions for P_1 and P_2 is shown Fig. 2(d).

We first focus on the SDP at the H point. As shown in Fig. 2(c), along the Γ -H path the bands split into four singlets with the irreducible representations of Γ_3 , Γ_1 , Γ_3 , Γ_1 and one doubly degenerate band of $\Gamma_2 + \Gamma_4$ representation of the C_{2v} symmetry. Along k -path H-N, the SDP splits into three doubly degenerate bands (nodal lines) with the $\Gamma_1 + \Gamma_2$ representation of the C_s symmetry. These nodal lines are protected by the glide mirror symmetry \tilde{M}_{110} and the time-reversal symmetry (T). We further construct an effective model for the SDP. The little group at the H point belongs to T_d , which can be generated from $\{\tilde{M}_{110} \mid \frac{1}{2}00\}$, $\{S_{4x}^{-1} \mid \frac{1}{2}00\}$, and $\{C_{3,1\bar{1}\bar{1}}^{-1} \mid 1\frac{11}{22}\}$. By choosing proper basis, the effective Hamiltonian of the SDP taking the following form:

$$H_{SDP}(\mathbf{k}) = \begin{pmatrix} h_{11}(\mathbf{k}) & h_{12}(\mathbf{k}) \\ h_{21}(\mathbf{k}) & h_{22}(\mathbf{k}) \end{pmatrix}. \quad (1)$$

Here, $h_{ij}(\mathbf{k})$ is a 3×3 matrix. Specifically,

$$h_{11}(\mathbf{k}) = \nu \mathbf{k} \cdot \mathbf{S}, \quad h_{12}(\mathbf{k}) = -\nu \mathbf{k} \cdot \mathbf{S}, \quad (2)$$

$$h_{12}(\mathbf{k}) = h_{21}^*(\mathbf{k}) = \begin{pmatrix} 0 & -\gamma' k_x & \gamma'' k_y \\ -\gamma'' k_x & 0 & \gamma' k_z \\ \gamma' k_y & \gamma'' k_z & 0 \end{pmatrix} \quad (3)$$

Here, ν is a real parameter. If we consider a limitation that $|\nu| \gg |\gamma'(\gamma'')|$, such a SDP carries a zero Chern number which is a composition of two spin-1 fermions. Here, we want to propose that, the SDP can be an excellent platform to realize other fermions such as eightfold-, fourfold-, and threefold fermion under SOC or lattice strain (see [Supplementary Information](#)).

Then, we turn to the FDP at the P point. As shown in Fig. 2(c), along the Γ -P-H path, the FDP splits into two singlets and one doubly degenerate band, which belong to the irreducible representations of Γ_1 , Γ_2 , and Γ_3 of the C_{3v} symmetry, respectively. Here we construct an effective model to obtain the topology of the FDP. The FDP at the P point is protected by the C_{3v} symmetry, which can be treated from

four independent generators including $\{S_{4x}^+ | \frac{1}{2}00\}$, $\{C_{3,\overline{1}\overline{1}1}^+ | 0\frac{11}{22}\}$, $\{C_{2y}^+ | 0\frac{11}{22}\}$, and $\{C_{2x}^+ | \frac{33}{22}0\}$. The FDP at the P point showing the irreducible representation of Γ_3 , and by combining the constraints of symmetries, the effective Hamiltonian up to the first order can be generally expressed as,

$$H_{FDP}(\mathbf{k}) = \begin{pmatrix} h_{11}(\mathbf{k}) & h_{12}(\mathbf{k}) \\ h_{21}(\mathbf{k}) & h_{22}(\mathbf{k}) \end{pmatrix}, \quad (4)$$

In details, each $h_{ij}(\mathbf{k})$ is a 2×2 matrix which can be given as,

$$h_{11}(\mathbf{k}) = v(k_x + ik_y)\sigma_+ + h.c., \quad h_{22}(\mathbf{k}) = -h_{11}(\mathbf{k}), \quad (5)$$

$$h_{12}(\mathbf{k}) = e^{i\theta_1} A k_z \sigma_z + [e^{i\theta_2} B (k_x + ik_y)\sigma_+ + h.c.], \quad h_{21}(\mathbf{k}) = h_{12}^*(\mathbf{k}).$$

Here, σ 's is the Pauli matrix, $\sigma_{\pm} = (\sigma_x \pm i\sigma_y)/2$. And, $\gamma = 3\alpha + \beta$, $A = \sqrt{(\alpha + \beta)^2 + 4\alpha^2}$, $B = \sqrt{2}\sqrt{4(\alpha - \beta)^2 + v^2}/4$, and parameters α and β are real which can be derived from DFT calculations. And θ_1 and θ_2 are real values: $\theta_1 = \arg[(\alpha + \beta) - i2\alpha]$, $\theta_2 = \arg[-2(\alpha - \beta) + i(3\alpha + \beta)] + \pi/4$.

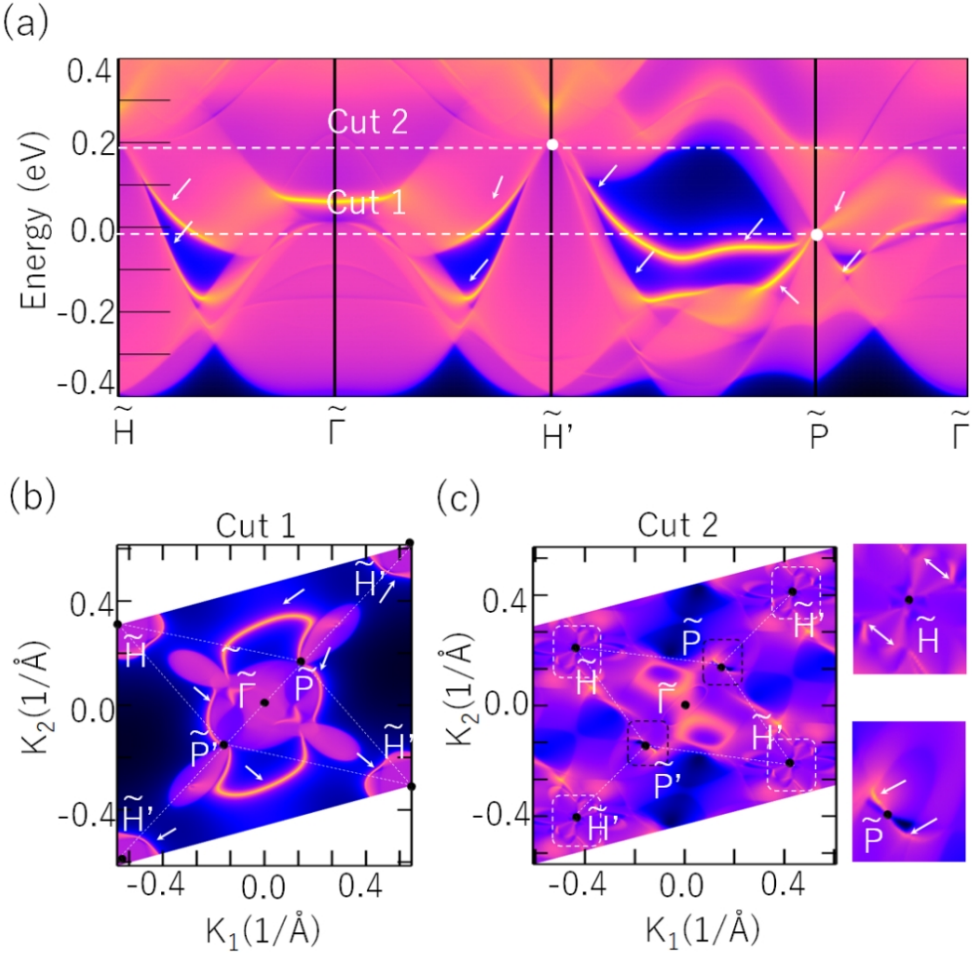
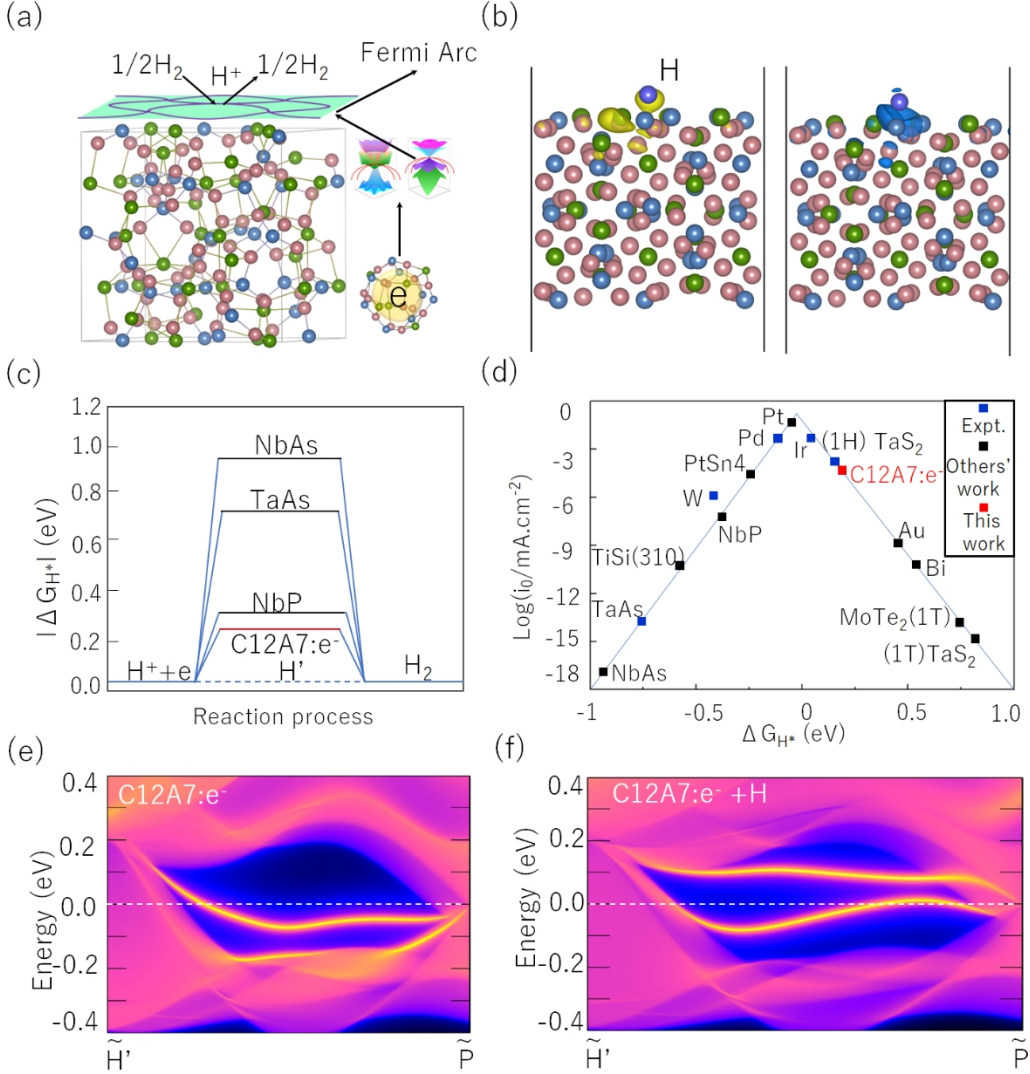


Fig. 3 (a) shows the (0 0 1) surface states of electride C12A7: e^- . (b) and (c) show the (001) surface slice under cut 1 (at energy of -0.01 eV) and cut 2 (0.19 eV), respectively. In (a), (b), (c), the Fermi arcs are pointed by the white arrows. In (c), the illustrations on the right panel are the partial enlarged view of the states in the white and black boxes.

Above discussions clarify C12A7: e^- is a topological electride with coexisting of SDP and FDP fermions. Here we investigate the potential surface states for these fermions. Figure 3(a) shows the (001) surface states along the surface paths shown in Fig. 1(c). We can observe two pieces of Fermi arc originating from the \tilde{H} (\tilde{H}') and \tilde{P} points. By showing the surface slices at the SDP and FDP fermions, we find the arcs of SDP show the dumbbell-like shape, and cover most region of (001) surface [see Fig. 3(a) and (c)]. For FDP, two pieces of Fermi arcs show the petal-like shape [see Fig. 3(a) and (b)]. Very interestingly, as shown Fig. 3(a), we find C12A7: e^- shows

extremely long Fermi arcs, nearly traversing the entire surface Brillouin zone.



Recently, nontrivial surface states in topological materials are believed to favor catalytic process with providing good conductivity, high electron mobility and low Gibbs free energy ⁷⁰⁻⁷⁷. Such materials, known as topological quantum catalysts, have been well demonstrated in several experiments performing on Weyl/Dirac semimetals TaAs, PtAl and PtSn₄ for HER ⁷⁰⁻⁷². Comparing with these examples, C12A7:e⁻ is different in two aspects: (1) C12A7:e⁻ is an electride, and the fermions are contributed by the excess electrons in the interstitial cites which are more loosely bounded; (2) C12A7:e⁻ possesses multiple-fold fermions (SDP and FDP), which show significantly longer Fermi arcs than Weyl/Dirac counterparts. These features may further enhance the activity for topological quantum catalysts.

For this consideration, we estimate the HER process on the (001) surface of C12A7:e⁻, as shown in Fig. 4(a). Here we use the ΔG_{H^*} of hydrogen adsorption on the catalyst surface to judge the HER activity. Just as expected, C12A7:e⁻ indeed shows a relatively low ΔG_{H^*} of 0.24 eV (see [Supplementary Information](#) for calculation details). As shown in Fig. 4(c), the absolute value $|\Delta G_{H^*}|$ in C12A7:e⁻ is significantly lower than those in Weyl catalysts NbP (0.31 eV), TaAs (0.74 eV) and NbAs (0.96 eV) ⁷⁰. Moreover, we plot the volcanic curves and compare the HER performance of electride C12A7:e⁻ with typical catalysts and topological quantum catalysts. As shown in Fig. 4(d), we find C12A7:e⁻ nearly situates at the top of the volcanic curves, indicating the surface of C12A7:e⁻ is highly active. In Fig. 4(e) and (f), we further compare the surface states of C12A7:e⁻ before and after hydrogen adsorption. We find the long Fermi arcs are robust during the HER process, but shift upward to the Fermi level. This indicates electride C12A7:e⁻ surface donates electrons to the *s* orbital of the adsorbed hydrogen. This process can also be traced from the charge density difference (CDD) in Fig. 4(b). We can find the charge depletion occurs on the surface of C12A7:e⁻, while charge accumulation happens around the adatom.

In addition, we have also estimated the ΔG_{H^*} inside the bulk cages, showing a

larger absolute value (0.51 eV) than the surface (0.24 eV). These results promise that the C12A7: e^- surface has a much higher activity for catalysis than the nano-sized cages inside the bulk. Our results are consistent with the findings in recent experiments performed on Ru/C12A7: e^- catalyst ⁶¹. Now, the fundamental mechanism on the enhanced activity in C12A7: e^- catalyst becomes clear: the bulk cages themselves are not active; however, the encaged excess electrons can contribute multiple-fold fermions. These fermions produce extremely long Fermi arcs and the highly active surface states. Our results provide fresh insights on understanding catalytic nature of electrides with nontrivial band topology.

In summary, we propose the presences of nontrivial band topology and multiple-fold fermions (including a SDP and a FDP) in electride C12A7: e^- . The multiple-fold fermions are formed by interstitial-electrons in the electride, being different from examples proposed in previous topological materials. The fermions are ensured by symmetry, and show novel surface states with long Fermi arcs nearly traversing the entire (001) surface Brillouin zone. The long Fermi arcs originating from the multiple-fold fermions make the C12A7: e^- (001) surface highly active, which provides a relatively low ΔG_{H^*} (0.24 eV) during the HER catalytic process. Notably, this ΔG_{H^*} is lower than most topological quantum catalysts proposed previously. Our work provides new understanding of the catalytic nature in C12A7: e^- -based catalysts by combining the topological quantum aspect.

Acknowledgements

This work is supported by National Natural Science Foundation of China (Grants No. 11904074). The work is funded by Science and Technology Project of Hebei Education Department, the Nature Science Foundation of Hebei Province (Nos. A2019202222 and A2019202107), the Overseas Scientists Sponsorship Program by Hebei Province (C20200319). The work is also supported by the State Key Laboratory of Reliability and Intelligence of Electrical Equipment (No. EERI_OY2020001), Hebei University of Technology. One of the authors (X.M.

Zhang) acknowledges the financial support from Young Elite Scientists Sponsorship Program by Tianjin.

References

- (1) Hasan, M. Z. and Kane C. L. Topological insulators. *Rev. Mod. Phys.* **2010**, *82*, 3045.
- (2) Qi, X.-L. and Zhang S.-C. Topological insulators and superconductors. *Rev. Mod. Phys.* **2011**, *83*, 1057.
- (3) Bansil, A.; Lin, H. and Das, T. Topological band theory. *Rev. Mod. Phys.* **2016**, *88*, 021004.
- (4) Chiu, C.-K.; Teo, J. C. Y.; Schnyder, A. P. and Ryu, S. Classification of topological quantum matter with symmetries. *Rev. Mod. Phys.* **2016**, *88*, 035005.
- (5) Yang, S. A. Dirac and Weyl materials: fundamental aspects and some spintronics applications. *SPIN* **2016**, *6*, 1640003.
- (6) Hasan, M. Z.; Xu, S.-Y. and Bian, G. Topological insulators, topological superconductors and Weyl fermion semimetals: discoveries, perspectives and outlooks. *Phys. Scr.* **2015**, *T164*, 014001.
- (7) Wan, X.; Turner, A. M.; Vishwanath, A. and Savrasov, S. Y. Topological semimetal and Fermi-arc surface states in the electronic structure of pyrochlore iridates. *Phys. Rev. B* **2011**, *83*, 205101.
- (8) Murakami, S. Phase transition between the quantum spin Hall and insulator phases in 3D: emergence of a topological gapless phase. *New J. Phys.* **2007**, *9*, 356.
- (9) Burkov A. A. and Balents, L. Weyl semimetal in a topological insulator multilayer. *Phys. Rev. Lett.* **2011**, *107*, 127205.
- (10) Young, S. M.; Zaheer, S.; Teo, J. C. Y.; Kane, C. L.; Mele, E. J. and Rappe, A. M. Dirac semimetal in three dimensions. *Phys. Rev. Lett.* **2012**, *108*, 140405.
- (11) Wang, Z.; Sun, Y.; Chen, X.-Q.; Franchini, C.; Xu, G.; Weng, H. M. Dai, X. and Fang, Z. Dirac semimetal and topological phase transitions in A_3Bi ($A=Na, K, Rb$). *Phys. Rev. B* **2012**, *85*, 195320.

(12) Wang, Z.; Weng, H. M.; Wu, Q.; Dai, X. and Fang, Z. Three-dimensional Dirac semimetal and quantum transport in Cd₃As₂. *Phys. Rev. B* **2013**, *88*, 125427.

(13) Yang, B.-J. and Nagaosa, N. Classification of stable three-dimensional Dirac semimetals with nontrivial topology. *Nat. Commun.* **2014**, *5*, 4898.

(14) Zhu, Z.; Winkler, G. W.; Wu, Q. S.; Li, J. and Soluyanov, A. A. Triple point topological metals. *Phys. Rev. X* **2016**, *6*, 031003.

(15) Weng, H. M.; Fang, C.; Fang, Z. and Dai, X. Topological semimetals with triply degenerate nodal points in θ-phase tantalum nitride. *Phys. Rev. B* **2016**, *93*, 241202.

(16) Bradlyn, B.; Cano, J.; Wang, Z.; Vergniory, M. et al. Beyond Dirac and Weyl fermions: Unconventional quasiparticles in conventional crystals. *Science* **2016**, *353*, aaf5037.

(17) Wieder, B. J.; Kim, Y.; Rappe, A. M. and Kane, C. L. Double Dirac semimetals in three dimensions. *Phys. Rev. Lett.* **2016**, *116*, 186402.

(18) Tang, P.; Zhou, Q. and Zhang, S.-C. Multiple types of topological fermions in transition metal silicides. *Phys. Rev. Lett.* **2017**, *119*, 206402.

(19) Chang, G. Q.; Xu, S.-Y.; Wieder, B. J. et al. Unconventional Chiral Fermions and Large Topological Fermi Arcs in RhSi. *Phys. Rev. Lett.* **2017**, *119*, 206401.

(20) Zhang, X.; Gu, Q. Q.; Sun, H. G.; Luo, T. C. et al. Eightfold fermionic excitation in a charge density wave compound. *Phys. Rev. B* **2020**, *102*, 035152.

(21) Kumar, N.; Yao, M. Y.; Nayak, J. et al. Signatures of Sixfold Degenerate Exotic Fermions in a Superconducting Metal PdSb₂. *Adv. Mater.* **2020**, *32*, 1906046.

(22) Mchröter, N. B. M.; Pei, D.; Vergniory, M. G. et al. Chiral topological semimetal with multifold band crossings and long Fermi arcs. *Nat. Phys.* **2019**, *15*, 759-765.

(23) Yuan, Q. Q.; Zhou, L. Q.; Rao, Z. C.; Tian, S. J. et al. Quasiparticle interference evidence of the topological Fermi arc states in chiral fermionic semimetal CoSi. *Sci. Adv.* **2019**, *5*, eaaw9485.

(24) Sun, Z. P.; Hua, C. Q.; Liu, X. L.; Liu, Z. T. et al. Direct observation of sixfold exotic fermions in the pyrite-structured topological semimetal PdSb₂. *Phys. Rev. B* **2020**, *101*, 155114.

(25) Yang, X.; Cochran, T. A.; Chapai, R.; Tristant, D. et al. Observation of sixfold degenerate fermions in PdSb_2 . *Phys. Rev. B* **2020**, *101*, 201105(R).

(26) Nie, S.; Bernevig, B. A.; Wang, Z. J. Six-fold Excitations in Electrides. arXiv:2006.12502.

(27) Dye, J. L.; Yemen, M. R.; DaGue, M. G. and Lehn, J.-M. Optical spectra of alkali metal anion and electride films, *J. Chem. Phys.* **1978**, *68*, 1665.

(28) J. L. Dye, Electrons as anions, *Science* **2003**, *301*, 607.

(29) Inoshita, T.; Jeong, S.; Hamada N. and Hosono, H. Exploration for Two-Dimensional Electrides via Database Screening and Ab Initio Calculation. *Phys. Rev. X* **2014**, *4*, 031023.

(30) Zhang, Y. Q.; Xiao, Z. W.; Kamiya, T. and Hosono, H. Electron confinement in channel spaces for one-dimensional electride. *J. Phys. Chem. Lett.* **2015**, *6*, 4966–4971.

(31) Ming, W.; Yoon, M.; Du, M.-H. et al. First-principles prediction of thermodynamically stable two-dimensional electrides. *J. Am. Chem. Soc.* **2016**, *138*, 15336–15344.

(32) Tsuji, Y.; Dasari, P. L. V. K.; Elatresh, S. F. et al. Structural Diversity and Electron Confinement in Li_4N : Potential for 0-D, 2-D, and 3-D Electrides. *J. Am. Chem. Soc.* **2016**, *138*, 14108–14120.

(33) Zhang, Y.; Wang, H.; Wang, Y.; Zhang, L. and Ma, Y. Computer Assisted Inverse Design of Inorganic Electrides. *Phys. Rev. X* **2017**, *7*, 011017.

(34) Dye, J. L. Electrides: Early Examples of Quantum Confinement. *Acc. Chem. Res.* **2009**, *42*, 1564–1572.

(35) Matsuishi, S.; Toda, Y., Masashi, M, et al. High-Density Electron Anions in a Nanoporous Single Crystal: $[\text{Ca}_{24}\text{Al}_{28}\text{O}_{64}]^{4+}(4\text{e}^-)$. *Science* **2003**, *301*, 626–629.

(36) Kim, S. W.; Shimoyama, T. and Hosono, H. Solvated Electrons in High-Temperature Melts and Glasses of the Room-Temperature Stable Electride $[\text{Ca}_{24}\text{Al}_{28}\text{O}_{64}]^{4+}\cdot 4\text{e}^-$. *Science* **2011**, *333*, 71–74.

(37) Toda, Y.; Yanagi, H.; Ikenaga, E.; Kim, J. J.; Kobata, M. et al. Solvated Electrons in High-Temperature Melts and Glasses of the Room-Temperature Stable Electride $[\text{Ca}_{24}\text{Al}_{28}\text{O}_{64}]^{4+} \cdot 4\text{e}^-$. *Adv. Mater.* **2007**, *19*, 3564–3569.

(38) Zhang, X.; Lei, H.; Toda, Y.; Matsuishi, S. et al. Two-Dimensional Transition-Metal Electride Y_2C . *Chem. Mater.* **2014**, *26*, 6638–6643.

(39) Xu, H. L.; Li, Z. R.; Wu, D. et al. Structures and Large NLO Responses of New Electrides: Li-Doped Fluorocarbon Chain. *J. Am. Chem. Soc.* **2007**, *129*, 2967–2970.

(40) Zhang, X. M.; Guo, R. K.; Jin, L.; Dai, X. F. and Liu G. D. Intermetallic Ca_3Pb : a topological zero-dimensional electride material. *J. Mater. Chem. C* **2018**, *6*, 575–581.

(41) Park, C.; Kim, S. W. and Yoon, M. First-Principles Prediction of New Electrides with Nontrivial Band Topology Based on One-Dimensional Building Blocks. *Phys. Rev. Lett.* **2018**, *120*, 026401.

(42) Hirayama, M.; Matsuishi, Satoru.; Hosono, Hideo. and Murakami, S. Electrides as a New Platform of Topological Materials. *Phys. Rev. X* **2018**, *8*, 031067.

(43) Blugel, S. and Mokrousov, Y. Two-Dimensional Topological Nodal Line Semimetal in Layered X_2Y ($\text{X} \frac{1}{4}$ Ca, Sr, and Ba; $\text{Y} \frac{1}{4}$ As, Sb, and Bi). *Phys. Rev. B* **2017**, *95*, 235138.

(44) Zhang, X. M.; Yu, Z. M.; Lu, Y. H; Sheng, X. L.; Yang, H. Y. and Yang, S. Y. A. Hybrid nodal loop metal: Unconventional magnetoresponse and material realization. *Phys. Rev. B* **2018**, *97*, 125143.

(45) Zhou, L.; Kou, L.; Sun, Y.; Felser, C.; Hu, F.; Shan, G. et al. New Family of Quantum Spin Hall Insulators in Two-Dimensional Transition-Metal Halide with Large Nontrivial Band Gaps. *Nano Lett.* **2015**, *15*, 7867.

(46) Dolui, K.; Ray, S. and Das, T. Intrinsic Large Gap Quantum Anomalous Hall Insulators in $\text{LaX}_\delta\text{X} \frac{1}{4}$ Br; Cl; I Φ . *Phys. Rev. B* **2015**, *92*, 205133.

(47) Wu, M. High-Temperature Intrinsic Quantum Anomalous Hall Effect in Rare Earth Monohalide. *2D Mater.* **2017**, *4*, 021014.

(48) Huang, H.; Jin, K.-H.; Zhang, S. and Liu, F. Topological Electride Y_2C , *Nano Lett.* **2018**, *18*, 1972.

(49) Matsuishi, S.; Toda, Y.; Miyakawa, M.; Hayashi, K.; Kamiya, T.; Hirano, M.; Tanaka, I.; Hosono, H. High-density electron anions in a nanoporous single crystal: $[\text{Ca}_{24}\text{Al}_{28}\text{O}_{64}]^{4+}(4\text{e}^-)$. *Science* **2003**, *301*, 626–9.

(50) Hayashi, K.; Matsuishi, S.; Kamiya, T.; Hirano, M.; Hosono, H. Light-induced Conversion of an Insulating Refractory Oxide into a Persistent Electronic Conductor. *Nature* **2002**, *419*, 462–465.

(51) Kim, S. W.; Shimoyama, T.; Hosono, H. Solvated Electrons in High-Temperature Melts and Glasses of the Room-Temperature Stable Electride $[\text{Ca}_{24}\text{Al}_{28}\text{O}_{64}]^{4+}\cdot 4\text{e}^-$. *Science* **2011**, *333*, 71–74.

(52) Toda, Y.; Yanagi, H.; Ikenaga, R.; Kim, J.-J.; Kobata, M.; Ueda, S. et al. Work Function of a Room-Temperature, Stable Electride $[\text{Ca}_{24}\text{Al}_{28}\text{O}_{64}]^{4+}(\text{e}^-)_4$. *Adv. Mater.* **2007**, *19*, 3564.

(53) Buchammangani, H.; Toda, Y.; Hirano, M.; Hosono, H.; Takeuchi, D.; Osakada, K. Room temperature-stable electride as a synthetic organic reagent: application to pinacol coupling reaction in aqueous media. *Org. Lett.* **2007**, *9*, 4287

(54) Kim, S.-W.; Matsuishi, S.; Nomura, T.; Kubota, Y.; Takata, M.; Hayashi, K.; Kamiya, T.; Hososno, H. Metallic state in a lime–alumina compound with nanoporous structure. *Nano Lett.* **2007**, *7*, 1138.

(55) Miyakawa, M.; Kim, S.-W.; Hirano, H.; Kohama, Y.; Kawaji, H.; Atake, T.; Ikegami, H.; Kono, K.; Hosono, H. Superconductivity in an Inorganic Electride $12\text{CaO}\cdot 7\text{Al}_2\text{O}_3\cdot \text{e}^-$. *J. Am. Chem. Soc.* **2007**, *129*, 7270–7271.

(56) Kitano, M.; Inoue, Y.; Yamazaki, Y.; Hayashi, F.; Kanbara, S.; Matsuishi, S.; Yokoyama, T.; Kim, S. W.; Hara, M.; Hosono, H. Ammonia synthesis using a stable electride as an electron donor and reversible hydrogen store. *Nat. Chem.* **2012**, *4* (11), 934–40.

(57) Inoue, Y. Kitano, M. Kim, S. W.; Yokoyama, T. et al. Highly Dispersed Ru on Electride $[\text{Ca}_{24}\text{Al}_{28}\text{O}_{64}]^{4+}(\text{e}^-)_4$ as a Catalyst for Ammonia Synthesis. *ACS Catal.* **2014**, *4*, 674-680.

(58) Kitano, M.; Kanbara, S.; Inoue, Y.; Kuganathan, N. et al. Electride support boosts nitrogen dissociation over ruthenium catalyst and shifts the bottleneck in ammonia synthesis. *Nat. Commun.* **2015**, *6* (1), 6731.

(59) Hara, M.; Kitano, M.; Hosono, H. Ru-Loaded C12A7: e^- Electride as a Catalyst for Ammonia Synthesis. *ACS Catal.* **2017**, *7* (4), 2313–2324.

(60) Ye, T. N.; Xiao, Z. W.; Li, J.; Gong, Y. T.; Abe, H. et al. Stable single platinum atoms trapped in subnanometer cavities in $12\text{CaO}\cdot7\text{Al}_2\text{O}_3$ for chemoselective hydrogenation of nitroarenes. *Nat. Commun.* **2020**, *11*, 1020.

(61) Kammert, J.; Moon, J.; Cheng, Y. Q.; Daemen, L. et al. Nature of Reactive Hydrogen for Ammonia Synthesis over a Ru/C12A7 Electride Catalyst. *J. Am. Chem. Soc.* **2020**, *142*, 7655-7667.

(62) Wu, J.; Gong, Y.; Inoshita, T.; Fredrickson, D. C.; Wang, J.; Lu, Y.; Kitano, M.; Hosono, H. Tiered Electron Anions in Multiple Voids of LaScSi and Their Applications to Ammonia Synthesis. *Adv. Mater.* **2017**, *29* (36), 1700924.

(63) Ogawa, T.; Kobayashi, Y.; Mizoguchi, H.; Kitano, M.; Abe, H.; Tada, T. et al. High Electron Density on Ru in Intermetallic YRu_2 : The Application to Catalyst for Ammonia Synthesis. *J. Phys. Chem. C* **2018**, *122* (19), 10468–10475.

(64) Tang, Y.; Kobayashi, Y.; Masuda, N.; Uchida, Y.; Okamoto, H.; Kageyama, T.; Hosokawa, S. et al. Metal-Dependent Support Effects of Oxyhydride-Supported Ru, Fe, Co Catalysts for Ammonia Synthesis. *Adv. Energy Mater.* **2018**, *8* (36), 1801772.

(65) Gao, W.; Guo, J.; Chen, P. Hydrides, Amides and ImidesMediated Ammonia Synthesis and Decomposition. *Chin. J. Chem.* **2019**, *37* (5), 442–451.

(66) Kitano, M.; Inoue, Y.; Ishikawa, H.; Yamagata, K.; Nakao, T.; Tada, T. et al. Essential role of hydride ion in ruthenium-based ammonia synthesis catalysts. *Chem. Sci.* **2016**, *7* (7), 4036–4043.

(67) Kresse, G. and Joubert, D. From ultrasoft pseudopotentials to the projector augmented-wave method. *Phys. Rev. B* **1999**, *59*, 1758.

(68) Nie, S. M. Qian, Y. T.; Gao, J. C.; Fang, Z. et al. The application of topological quantum chemistry in electrides. arXiv:2012.02203.

(69) Bradlyn, B.; Elcoro, L.; Cano, J.; Vergniory, M.; Wang, Z. et al. Topological quantum chemistry. *Nature* **2017**, *547*, 298.

(70) Rajamathi, C. R.; Gupta, U.; Kumar, N.; Yang, H. et al. Weyl semimetals as hydrogen evolution catalysts. *Adv. Mater.* **2017**, *29*, 1606202.

(71) Yang, Q. Li, G. W. Manna, K. Fan, F. R. et al. Topological Engineering of Pt-Group-Metal-Based Chiral Crystals toward High-Efficiency Hydrogen Evolution Catalysts, *Adv. Mater.* **2020**, *32*, 1908518.

(72) Li, G. Fu, C.; Shi, W.; Jiao, L.; Wu, J.; Yang, Q.; et al. Dirac Nodal Arc Semimetal PtSn₄: An Ideal Platform for Understanding Surface Properties and Catalysis for Hydrogen Evolution. *Angew. Chem., Int. Ed.* **2019**, *58*, 13107.

(73) Li, G.; Xu, Q.; Shi, W.; Fu, C.; Jiao, L.; Kamminga, M. E. et al. Surface states in bulk single crystal of topological semimetal Co₃Sn₂S₂ toward water oxidation. *Sci. Adv.* **2019**, *5*, eaaw9867.

(74) Xiao, J. P.; Kou, L. Z.; Yam, C. Y.; Frauenheim, T.; Yan, B. H. Toward Rational Design of Catalysts Supported on a Topological Insulator Substrate. *ACS Catal.* **2015**, *5*, 7063-7067.

(75) Li, J.; Ma, H.; Xie, Q.; Feng, S.; Ullah, S. et al. Topological quantum catalyst: Dirac nodal line states and a potential electrocatalyst of hydrogen evolution in the TiSi family. *Sci. China Mater.* **2018**, *61*, 23.

(76) Li, L.; Zeng, J.; Qin, W.; Cui, P.; Zhang, Z. Tuning the hydrogen activation reactivity on topological insulator heterostructures. *Nano Energy* **2019**, *58*, 40.

(77) Li, G. W.; Felser, C. Heterogeneous catalysis at the surface of topological materials. *Appl. Phys. Lett.* **2020**, *116*, 070501.

(78) Hinnemann, B.; Moses, P. G.; Bonde, J. et al. Biomimetic hydrogen evolution: MoS₂ nanoparticles as catalyst for hydrogen evolution. *J. Am. Chem. Soc.* **2005**, *127*, 5308–5309.

(79) Greeley, J.; Jaramillo, T. F.; Bonde, J. et al. Computational high throughput screening of electrocatalytic materials for hydrogen evolution. *Nat Mater.* **2006**, *5*, 909–913.